Article

Tracking cubic ice at molecular resolution

https://doi.org/10.1038/s41586-023-05864-5

Received: 7 July 2022

Accepted: 17 February 2023

Published online: 29 March 2023

Check for updates

Xudan Huang[1,2,8], Lifen Wang[1,3,8]✉, Keyang Liu[4,8], Lei Liao[1,2], Huacong Sun[1,2], Jianlin Wang[1,2], Xuezeng Tian[1], Zhi Xu[1,3], Wenlong Wang[1,3], Lei Liu[5,6], Ying Jiang[4,6], Ji Chen[4,6,7]✉, Enge Wang[1,3,4,6]✉ & Xuedong Bai[1,2,3]✉

Ice is present everywhere on Earth and has an essential role in several areas, such as cloud physics, climate change and cryopreservation. The role of ice is determined by its formation behaviour and associated structure. However, these are not fully understood[1]. In particular, there is a long-standing debate about whether water can freeze to form cubic ice—a currently undescribed phase in the phase space of ordinary hexagonal ice[2–6]. The mainstream view inferred from a collection of laboratory data attributes this divergence to the inability to discern cubic ice from stacking-disordered ice—a mixture of cubic and hexagonal sequences[7–11]. Using cryogenic transmission electron microscopy combined with low-dose imaging, we show here the preferential nucleation of cubic ice at low-temperature interfaces, resulting in two types of separate crystallization of cubic ice and hexagonal ice from water vapour deposition at 102 K. Moreover, we identify a series of cubic-ice defects, including two types of stacking disorder, revealing the structure evolution dynamics supported by molecular dynamics simulations. The realization of direct, real-space imaging of ice formation and its dynamic behaviour at the molecular level provides an opportunity for ice research at the molecular level using transmission electron microscopy, which may be extended to other hydrogen-bonding crystals.

Cubic ice (ice Ic) has a diamond- cubic structure with a repeating face-centred cubic array of tetrahedrally coordinated water molecules (Fig. 1a). Scheiner's halo suggests the existence of ice Ic in nature[3]. Extensive laboratory research efforts have aimed to prepare ice Ic using complex approaches, including freezing aqueous droplets[5], heating vitrified water[12], confining water in mesopores[13], thermal treatment of high-pressure phases of pure ice[4,14,15] and disruption of gas hydrate[16–18]. But these experiments did not convincingly demonstrate a cubic phase in pure state and are now widely accepted to show stacking-disordered ice[11] (ice Isd). Recently, pure ice Ic crystals were synthesized in the laboratory by heating ice XVII to 160 K under vacuum[19] or degassing a C_2 hydrogen hydrate at 100 K (ref. [20]). With accumulating evidence, the demonstrated existence and metastability of the pure ice Ic may challenge the present interpretation of ice Isd that assumes that metastable ice Ic and stable hexagonal ice (ice Ih) can coexist.

The structural characterization of ice is usually based on diffraction methods that provide spatially averaged information. Scanning probe microscopy has enabled atomic-level structural characterization of ultrathin ice[21], but only of the topmost one or two layers. Although electron microscopy is also capable of atomic-resolution structural imaging, its application to ice is challenging because of the difficulty in preparing samples stable under low-pressure imaging conditions and while exposed to electron beams. Moreover, some supporting substrates will interfere with the imaging of oxygen columns in ice. These challenges explain the limited use of transmission electron microscopy (TEM) when studying ice, with only transient imaging of bulk single-crystalline Ih reported because samples degrade under electron beam irradiation[22].

To enable TEM imaging, residual water vapour present in the TEM columns is deposited onto cryogenic TEM grids. A low-dose imaging technique was used to capture the depositions (Fig. 1b, Methods and Extended Data Fig. 1). Sequential TEM images and corresponding fast Fourier transform (FFT) showed that amorphous solid water[23] deposited first, after which the ice Ic nucleus formed, which had a single-crystalline lattice along the <110> zone axis (Fig. 1c). The measured lattice constant *a* was 6.36 Å, similar to the diffraction value of 6.37451 Å for heavy-water ice Ic (ref. [19]). Subsequently, the ice Ic nucleus grew to a faceted crystallite in a matter of hours (Fig. 1d). This type of ice Ic crystallization event represents most of the observed heterogeneous ice nucleation process (Extended Data Fig. 2). The collected growth profiles shown in Fig. 1e demonstrated that the size of the obtained ice Ic in each dimension was mostly in the nanometre range, with a lifespan longer than TEM experimental hours.

The on-site acquired electron energy loss spectroscopy (EELS) results showed two peaks arising over time during the cryogenic process on the graphene substrate, including one peak (peak I) at 8.8 eV that agrees well with the reported electronic gap of ice[24] and an accompanying accumulating peak at 532 eV for the oxygen K-edge (Fig. 1f). The K-edge for carbon at 284 eV gradually declined, implying an increase in carbon-free deposit. Consistently, the peak at 15.6 eV for the monolayer graphene shifted to 21 eV, which is assigned to the bulk ice plasmon, confirming ice adsorption.

[1]Beijing National Laboratory for Condensed Matter Physics, Institute of Physics, Chinese Academy of Sciences, Beijing, China. [2]School of Physical Sciences, University of Chinese Academy of Sciences, Chinese Academy of Sciences, Beijing, China. [3]Songshan Lake Materials Laboratory, Dongguan, China. [4]School of Physics, Peking University, Beijing, China. [5]School of Materials Science and Engineering, Peking University, Beijing, China. [6]Interdisciplinary Institute of Light-Element Quantum Materials and Research Center for Light-Element Advanced Materials, Peking University, Beijing, China. [7]Frontiers Science Center for Nano-Optoelectronics, Peking University, Beijing, China. [8]These authors contributed equally: Xudan Huang, Lifen Wang, Keyang Liu. ✉e-mail: wanglf@iphy.ac.cn; ji.chen@pku.edu.cn; egwang@pku.edu.cn; xdbai@iphy.ac.cn

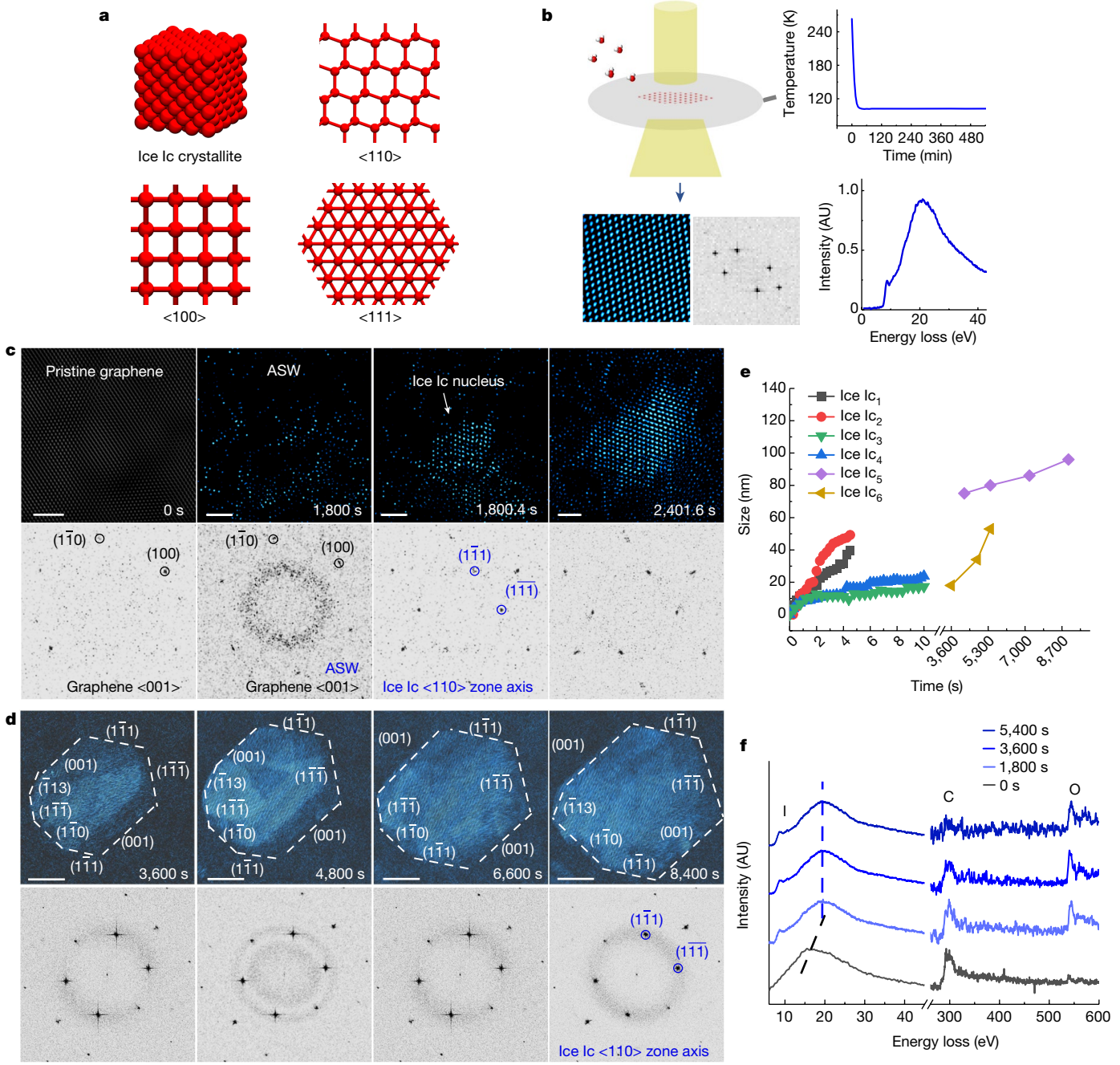

Fig. 1 | Visualization of heterogeneous nucleation and growth of ice Ic using in situ low-dose cryogenic TEM. a, The ice Ic structure along different perspective directions. **b**, Experimental set-up for in situ cryogenic TEM. The temperature was measured and recorded while the monolayer graphene on one TEM grid was frozen. Simultaneously, residual water vapour in the TEM vacuum chamber condensed on the cryogenic graphene as ice and was then characterized by TEM, including imaging and EELS. **c**,**d**, A set of representative in situ real-time TEM images (top) and corresponding FFTs (bottom) showing amorphous solid water that formed on the graphene substrate first, followed by ice Ic nucleation and facet growth. The start time was defined as the time when the substrate started to cool down. Each image was obtained by summing eight aligned frames in one corresponding low-dose image stack acquired at a frame rate of 40 frames per second with a total irradiation time of 2 s and a dose rate of 120 e^{-} Å^{-2} s^{-1} (Extended Data Fig. 1). **e**, Size growth profiles describing the progress of water vapour freezing to nanometre-sized ice Ic crystallites (Extended Data Fig. 2). **f**, Sequential real-time dual-EELS spectra with both low loss and core loss of the cooling substrate, showing a new peak I arising at 8.8 eV ascribed to the electronic interband transition of bulk ice. The pristine plasmon peak at 15.6 eV belonging to monolayer graphene that gradually shifted to 21 eV was attributed to bulk ice plasmon. AU, arbitrary units. Scale bars, 2 nm (**c**) and 20 nm (**d**).

Given that the pure-phase single crystalline ice Ic crystallites were consistently spotted in nucleation and growth, the low temperature and low pressure were conducive to heterogeneous ice Ic nucleation. Our examination of ice depositions on different substrates (Fig. 2) further demonstrated that substrates other than graphene can also be effective for the heterogeneous nucleation of ice Ic.

Figure 2a–d shows four representative ice crystals with distinct but well-defined polyhedral morphologies found on different substrates, including hydrophobic carbon, hydrophilic carbon, graphene and hexagonal boron nitride (h-BN). High-magnification TEM images showed that these isolated crystallites were all single crystals without notable defects (Fig. 2e–h). The measured consistent lattice constant of 6.36 Å

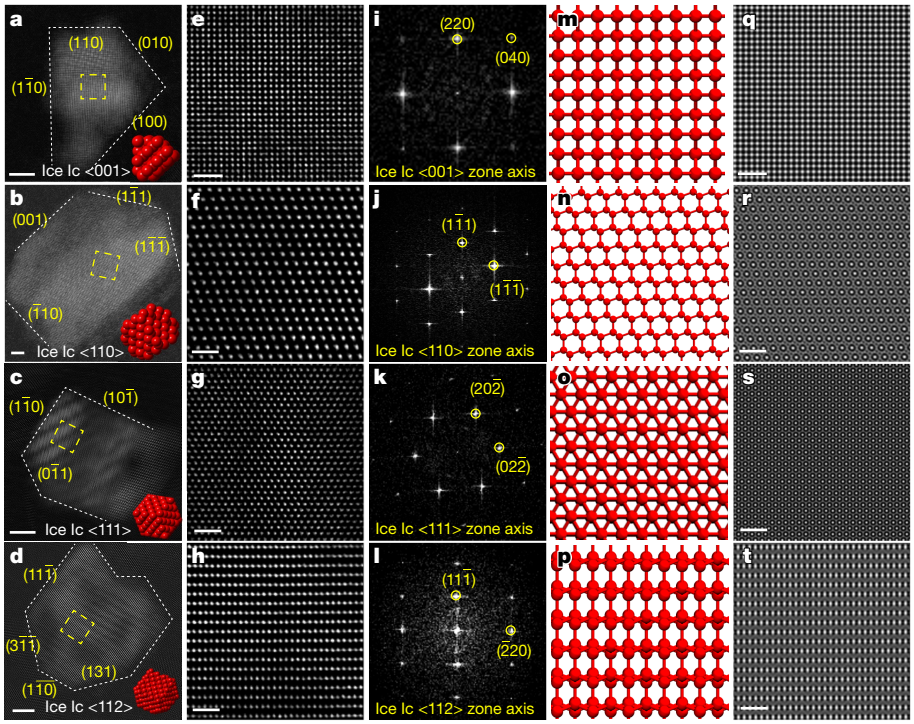

Fig. 2 | Single-crystalline ice Ic crystallites grown on different substrates. **a**–**d**, Low-magnification TEM images of individual crystallites, including hydrophobic carbon (**a**), hydrophilic carbon (**b**), graphene (**c**) and monolayer h-BN (**d**). A polyhedron-truncated ice Ic cube along the corresponding view direction is included. **e**–**h**, High-magnification micrographs of the highlighted areas in **a**–**d** showing single-crystalline lattice without defects. **i**–**l**, Corresponding FFTs of the images in **a**–**d**, indicating a single-crystalline structure as indexed by ice Ic along four crystallography orientations. **m**–**p**, Ice Ic lattice schematics corresponding to the images in **e**–**h**. **q**–**t**, Computed TEM images of ice Ic lattices with a thickness of 15 nm (**q**), 30 nm (**r**), 15 nm (**s**) and 20 nm (**t**) in the images from **m**–**p** show good agreement with the experimental images shown in **e**–**h**. Scale bars, 10 nm (**a**–**d**), 1 nm (**e**–**h**) and 1 nm (**q**–**t**). Electron doses, 54 e^- Å^{-2} (**a**,**e**), 44 e^- Å^{-2} (**b**,**f**), 40 e^- Å^{-2} (**c**,**g**) and 56 e^- Å^{-2} (**d**,**h**). Electron irradiation time, 0.4 s (**a**–**h**).

corroborated that these faceted crystallites were ice Ic crystallites along the <001>, <110>, <111> and <112> crystallography orientations (Fig. 2i–l). The facets and diffraction spots of these crystallites were therefore indexed. Notably, the nanometre size of the crystallites caused the broadening of the diffraction spots. Furthermore, a few fake weak spots were generated because of the low signal-to-noise ratio caused by the poor scattering power of the water molecules. The atomic structure models were built (Fig. 2m–p) and image simulations were performed (Fig. 2q–t and Methods) for comparison. The models and simulations demonstrated results that were consistent with those of the experimental observations. Thus, the observed pure-phase single crystals fully demonstrate the heterogeneous nucleation of pure-phase ice Ic at the current conditions.

In addition to the dominating ice Ic crystallites, a small amount of ice Ih and one orthorhombic ice XI crystallite[25] (due to electron beam charging[26]) were also found, revealing the polymorphic diversity of ice crystallization (Extended Data Figs. 3–7). Ice Ih directly nucleated from amorphous solid water. No phase transition from the cubic to hexagonal phase was observed because of the metastability of ice Ic under the present thermodynamic conditions. Therefore, the sequential diffraction intensity profile of this nucleus mixture with distinct structures in separate crystallization pathways showed evolving peaks (Extended Data Fig. 8). This profile is similar to the diffraction pattern obtained with a broad range of well-studied conditions, assuming monodispersed particles, that were previously interpreted[11] as Isd. Usually, owing to the probe size and signal-to-noise ratio requirements, a sample of common diffraction approaches contains dozens or more nanoparticles. The observed variation in the acquired structural composition over time, sampling and substrate explains the similar, albeit not identical, diffraction patterns obtained in similar vapour deposition experiments[2,26]. The observed polymorphic complexity of ice nuclei emphasizes the importance of real-space imaging for reliable structure and crystallization pathway determinations.

On the basis of the consistency of ice Ic and ice Ih in the water tetrahedron as a common constituent unit, the difference in Gibbs free energy that determines the thermodynamic preference among the two polymorphs is minor, with a slightly more favourable value for Ih than for Ic (refs. [7,10]). Because the real-time observation showed that the vast majority of the nascent heterogeneous nuclei comprises ice Ic, it is highly probable that the interfacial free energy—which is influenced by polymorph-dependent interface characters[27], such as the surface tension and interplay between the nucleus and substrate—is in favour of ice Ic, leading to the nucleation preference for ice Ic at small sizes. This preferential nucleation of ice Ic caused by the interface effects corroborates the previous experimental study[28] in which nanopore condensation produced mainly ice Ic. Parallel to this, the nucleation of ice Ic has recently been shown to have a high degree of adaptability and robustness to both substrate deformations and system size changes in simulations[29]. Ice crystallization may vary widely under distinct conditions, the influence that the varying conditions of supersaturation and supercooling may have on the outset and the evolution of polymorphic diversity for heterogeneous ice nucleation, requires detailed and statistical studies in the future.

While screening the crystal structure of ice crystallites, the direct, high-resolution imaging of ice at the molecular level further allowed us to investigate the microscopic defects that occur in ice Ic. The observed defects were categorized into two types depending on whether they introduce stacking-disorder domains in the ice Ic matrix (Fig. 3). Type-1 defects (Fig. 3a–h) feature planar defects confined to a close-packed {111} plane, including twinning (blue line), stacking faults (yellow lines) and their intersections. Type-2 defects (Fig. 3i–k) are domain disorders

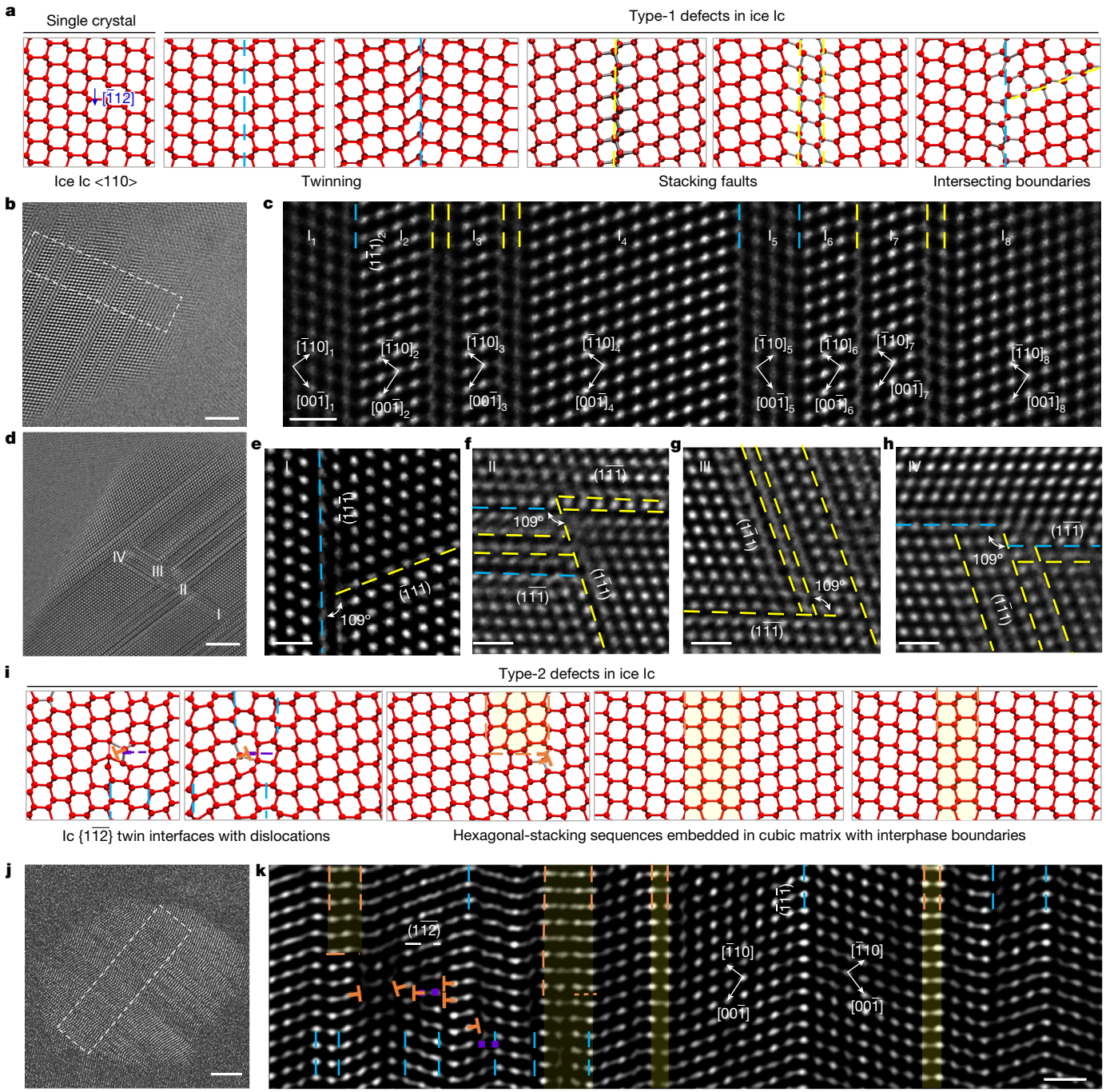

Fig. 3 | Defects in ice Ic crystallites. a, Atomic structures of single-crystal ice Ic <110> and type-1 defects. All structures were relaxed using the mW water model. Twinning and stacking faults are highlighted by blue and yellow dashed lines, respectively. **b**, TEM micrograph of one ice Ic crystallite with a high density of type-1 defects. **c**, TEM image of the area highlighted in **b** showing the atomic configurations of the type-1 defects. **d**, TEM image of a defective ice Ic crystallite. **e**–**h**, High-magnification images of areas I–IV in **d**, showing intersecting boundary configurations at the junctions. **i**, Atomic structure illustrations of type-2 defects. Hexagonal regions are coloured in yellow. **j**, TEM image of a defective ice crystallite. **k**, High-magnification TEM image of the area circled in **j** showing type-1 and type-2 defect configurations. Scale bars, 5 nm (**b**,**d**,**j**) and 1 nm (**c**,**e**–**h**,**k**). Electron irradiation time, 0.4 s (**b**–**h**,**j**,**k**). Electron doses, 62.4 e^{-} $Å^{-2}$ (**b**,**c**), 51.2 e^{-} $Å^{-2}$ (**d**–**h**) and 39.2 e^{-} $Å^{-2}$ (**j**,**k**).

with defects in one area, such as twinning interfacing with misfit dislocations (purple lines) and hexagonal close-packed sequences—that is, the Ih domain (yellow colour) with accompanying interphase boundaries (orange lines).

We found type-1 defects embedded in an ice Ic crystallite that gave rise to a nanolamellar structure (Fig. 3b). The high-magnification TEM image (Fig. 3c) showed clearly defined type-1 defect configurations, in which the long-period cubic-stacking sequences were disturbed by planar interfaces. Moreover, water-dimer columns in the fault ice layer showed an indistinct and thread-like distribution, in contrast to the clearly defined spots that were evenly spread out on one flat plane such as in an ice Ic lattice. Molecular dynamics simulations showed that the triangular water pyramids in the fault layer adapted to distortions in the hydrogen bond length and angle to release the misfit stress (Fig. 3a). We also found that these planar defects can intersect each other, separating one crystallite into eight nanograins with four junction boundaries

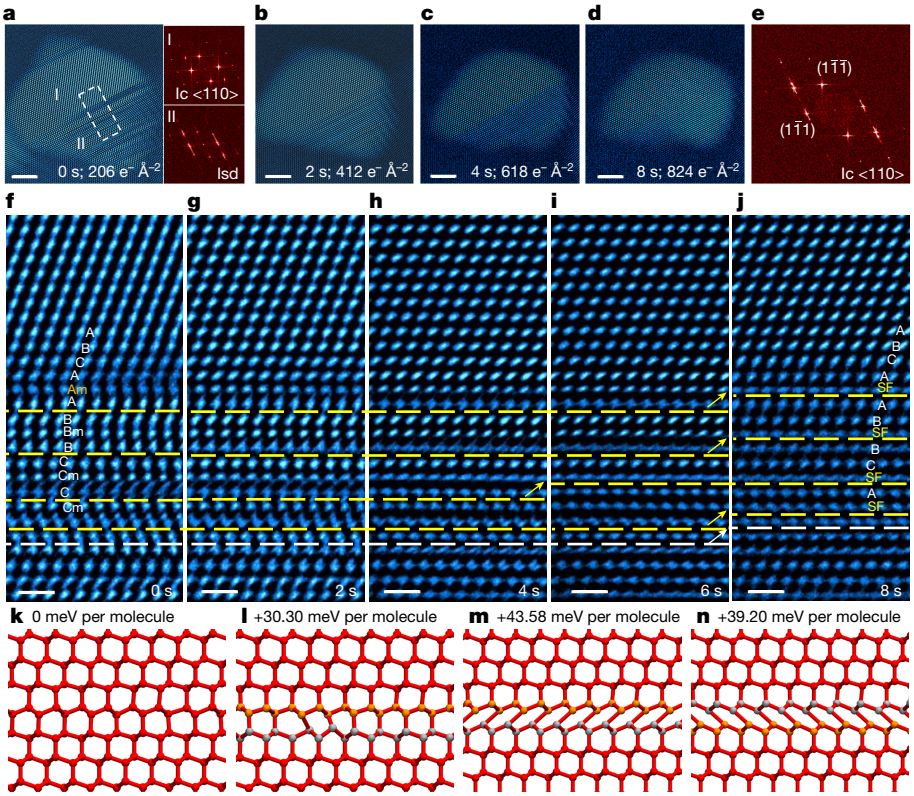

Fig. 4 | Structural dynamics of stacking disorders in ice Ic. a, TEM image and corresponding selected area FFTs of an ice Ic crystallite showing stacking disorder in area II. The transmitted electron beam dose for the micrograph is included. **b**–**d**, Sequential snapshot micrographs of the crystallite showing that its shrinking size is accompanied by microstructure evolution. The accumulated illumination electron dose is included. **e**, Corresponding FFT of the image in **d** showing ice Ic along the <110> zone axis. **f**–**j**, Time-lapsed high-magnification TEM images of the area marked by a rectangle in **a** showing structural evolution (Supplementary Video 1). Yellow dashed lines mark stacking-disordered layers that first distorted and then climbed up a layer after electron irradiation. White line marks the twin interface that also climbed up a layer. **k**–**n**, Defect configuration snapshot and corresponding energy barrier from nudged elastic band calculations, showing the defect structural dynamics and evolution kinetic pathway. Scale bars, 5 nm (**a**–**d**) and 1 nm (**f**–**j**). Electron irradiation time, 0.4 s (**a**–**d**,**f**–**j**).

(Fig. 3d). Figure 3e–h shows the high-magnification images of these junctions with junction angles of approximately 109°.

Figure 3i shows a schematic of type-2 defects. A low-magnification image showed a high density of defects in a nanometre-sized ice crystallite (Fig. 3j). The molecular-resolution micrograph shown in Fig. 3k showed that the crystallite was composed of a big ice Ic lattice area with type-1 defects and several disordered domains. Type-2 defect configurations in the disordered areas were clearly identifiable. The twinning of the cubic array oriented along the <110> zone axis on the $\{1\bar{1}\bar{2}\}$ plane introduced a high density of misfit dislocations. An interphase boundary between the hexagonal domain and the cubic matrix on the $\{1\bar{1}\bar{2}\}_c$ plane had another misfit dislocation. Some hexagonal and cubic layers were alternately stacked along the closely packed direction.

The pure hexagonal stacking domains in the TEM micrograph showed a plane-symmetrical stacking pattern. Although the hexagonal domain mostly contained only two adjoint ice layers and the uneven distribution in the cubic matrix was small, the domain was verified, thus identifying another ice I polytype, Isd. The cubicity—that is, the proportion of cubic sequences—was estimated to be 86% of the observed ice Isd crystallite. Although defective ice Ic crystallites were found with the propensity of grown-in twinning and stacking faults, this stacking-faulted ice Isd formed under the complex competitive nucleation of ice Ic and ice Ih raises the question of whether this unique polymorph can initiate the transition from Ic to Ih on energy perturbations.

We investigated the structural dynamics of stacking disorders in ice Ic further (Fig. 4). Figure 4a reveals a pristine ice crystallite that was composed of a defect-free Ic domain (area I) and a stacking-disordered domain (area II). In the following experiments, the illumination electron beam dose rate was slightly increased to accelerate the local energy transfer from the electron beam to the ice structure. Consequently, the surfaces of the crystallite peeled off layer by layer, which suggests sublimation (Fig. 4b–d). Area II, which initially showed a striped lattice, gradually showed a changing fringe distribution with increasing irradiation time, suggesting the internal instability of this defect structure. The FFT (Fig. 4e) corresponding to Fig. 4d revealed that the evolved crystallite still maintained the ice Ic configuration in the matrix.

Sequential molecular-resolution TEM images further resolved the microscopic details of the dynamic process (Fig. 4f–j and Supplementary Video 1). For instance, the ice layer denoted as A and marked by a yellow line in Fig. 4f initially formed a hexagonal stack with the top two ice layers and a cubic stack with its bottom ice layer. Under continuous electron beam irradiations, the originally smooth spots—that is, the water-dimer columns in the ice layer—became distorted (Fig. 4g), suggesting the deformation of the triangular water pyramids in the layer. The distortion gradually increased (Fig. 4h), reached its maximum state (Fig. 4i) and then disappeared in the A layer (Fig. 4i). Moreover, the upper adjacent A_m layer first moved slightly in the horizontal <$\bar{1}$12> direction, and finally showed an obvious distortion, indicating the climbing of the stacking fault (Fig. 4i,j). This collaborative deformation process of first intralayer distortion and then interlayer climbing was applicable to the defect layers. The ice Ic twin boundary also climbed under electron beam irradiation as marked by the white lines (Fig. 4f–j). The structural instability of the ice Ic defects and a preference for a {111} slip system were thus observed.

The stacking-disorder evolution pathway and the corresponding potential energy map were further evaluated using molecular dynamics simulations (Methods). Figure 4l shows that the collaborative distortions in the interface layer and the adjoint hexagonal layer require 30.30 meV per molecule, corresponding to the initial distortion in Fig. 4g. The estimated energy barrier for the maximum distortion in the stacking fault bilayer was 45.38 meV per molecule (Fig. 4m). A major distortion in the middle hexagonal close-packed layer, such as the stacking fault configuration in Fig. 4j, needed 39.20 meV per molecule (Fig. 4n). The in situ images showed continuous sublimation of the surface ice, confirming that the energy transferred from the 300-kV accelerated electron beam to the water molecules exceeds the surface-water displacement energy of 0.5 eV (Methods). The low-energy barriers of the transition between different lattice defects are thus surmountable, hence explaining the experimentally observed structural evolution pathway based on energy considerations. The examination of the structure and dynamics of defects in ice Ic provides a key step towards understanding the plasticity of ice at the molecular level.

It is important to clarify that the evolution of the defects in defective ice Ic, either during growth (Extended Data Figs. 9 and 10) or under electron beam irradiation, does not drive the solid-sate phase transition from ice Ic to ice Ih. Such robust stability of ice Ic is highly consistent with its high competitiveness, which has been demonstrated in heterogeneous nucleation and crystallization processes. This further corroborates that ice Ic formed by preferential nucleation at low-temperature interfaces has a sound thermodynamic stability. As a possible extension, heterogeneous ice Ic may be omnipresent at low temperatures because of the abundance and ubiquity of interfaces. Future in-depth examination of ice I formation behaviour related to polymorphic competition associated with the interface effect would greatly enhance our understanding of ice I, thus warranting further experimental and theoretical investigations.

Online content

Any methods, additional references, Nature Portfolio reporting summaries, source data, extended data, supplementary information, acknowledgements, peer review information; details of author contributions and competing interests; and statements of data and code availability are available at https://doi.org/10.1038/s41586-023-05864-5.

1. Bartels-Rausch, T. Ten things we need to know about ice and snow. *Nature* **494**, 27–29 (2013).
2. König, H. Eine kubische Eismodifikation. *Z. Kristallogr. Cryst. Mater.* **105**, 279–286 (1943).
3. Whalley, E. Scheiner's halo: evidence for ice Ic in the atmosphere. *Science* **211**, 389–390 (1981).
4. Kuhs, W., Bliss, D. & Finney, J. High-resolution neutron powder diffraction study of ice Ic. *J. Phys. Colloq.* **48**, C1-631–C1-636 (1987).
5. Mayer, E. & Hallbrucker, A. Cubic ice from liquid water. *Nature* **325**, 601–602 (1987).
6. Murray, B. J., Knopf, D. A. & Bertram, A. K. The formation of cubic ice under conditions relevant to Earth's atmosphere. *Nature* **434**, 202–205 (2005).
7. Moore, E. B. & Molinero, V. Is it cubic? Ice crystallization from deeply supercooled water. *Phys. Chem. Chem. Phys.* **13**, 20008–20016 (2011).
8. Kuhs, W. F., Sippel, C., Falenty, A. & Hansen, T. C. Extent and relevance of stacking disorder in "ice I_c". *Proc. Natl Acad. Sci. USA* **109**, 21259–21264 (2012).
9. Malkin, T. L., Murray, B. J., Brukhno, A. V., Anwar, J. & Salzmann, C. G. Structure of ice crystallized from supercooled water. *Proc. Natl Acad. Sci. USA* **109**, 1041–1045 (2012).
10. Lupi, L. et al. Role of stacking disorder in ice nucleation. *Nature* **551**, 218–222 (2017).
11. Malkin, T. L. et al. Stacking disorder in ice I. *Phys. Chem. Chem. Phys.* **17**, 60–76 (2015).
12. McMillan, J. A. & Los, S. C. Vitreous ice: irreversible transformations during warm-up. *Nature* **206**, 806–807 (1965).
13. Morishige, K. & Uematsu, H. The proper structure of cubic ice confined in mesopores. *J. Chem. Phys.* **122**, 044711 (2005).
14. Arnold, G. P., Finch, E. D., Rabideau, S. W. & Wenzel, R. G. Neutron-diffraction study of ice polymorphs. III. Ice Ic. *J. Chem. Phys.* **49**, 4365–4369 (1968).
15. Bertie, J. E., Calvert, L. D. & Whalley, E. Transformations of ice II, ice III, and ice V at atmospheric pressure. *J. Chem. Phys.* **38**, 840–846 (1963).
16. Kuhs, W. F., Genov, G., Staykova, D. K. & Hansen, T. Ice perfection and onset of anomalous preservation of gas hydrates. *Phys. Chem. Chem. Phys.* **6**, 4917–4920 (2004).
17. Falenty, A. & Kuhs, W. F. "Self-preservation" of CO_2 gas hydrates—surface microstructure and ice perfection. *J. Phys. Chem. B* **113**, 15975–15988 (2009).
18. Ghosh, J., Bhuin, R. G., Vishwakarma, G. & Pradeep, T. Formation of cubic ice via clathrate hydrate, prepared in ultrahigh vacuum under cryogenic conditions. *J. Phys. Chem. Lett.* **11**, 26–32 (2020).
19. del Rosso, L. et al. Cubic ice Ic without stacking defects obtained from ice XVII. *Nat. Mater.* **19**, 663–668 (2020).
20. Komatsu, K. et al. Ice I_c without stacking disorder by evacuating hydrogen from hydrogen hydrate. *Nat. Commun.* **11**, 464 (2020).
21. Ma, R. et al. Atomic imaging of the edge structure and growth of a two-dimensional hexagonal ice. *Nature* **577**, 60–63 (2020).
22. Kobayashi, K., Koshino, M. & Suenaga, K. Atomically resolved images of I_h ice single crystals in the solid phase. *Phys. Rev. Lett.* **106**, 206101 (2011).
23. Mishima, O., Calvert, L. D. & Whalley, E. 'Melting ice' I at 77 K and 10 kbar: a new method of making amorphous solids. *Nature* **310**, 393–395 (1984).
24. Pan, D., Wan, Q. & Galli, G. The refractive index and electronic gap of water and ice increase with increasing pressure. *Nat. Commun.* **5**, 3919 (2014).
25. Tajima, Y., Matsuo, T. & Suga, H. Phase transition in KOH-doped hexagonal ice. *Nature* **299**, 810–812 (1982).
26. Kobayashi, K. & Yasuda, H. Phase transition of ice I_c to ice XI under electron beam irradiation. *Chem. Phys. Lett.* **547**, 9–12 (2012).
27. Małolepsza, E. & Keyes, T. Water freezing and ice melting. *J. Chem. Theory Comput.* **11**, 5613–5623 (2015).
28. Steytler, D. C., Dore, J. C. & Wright, C. J. Neutron diffraction study of cubic ice nucleation in a porous silica network. *J. Phys. Chem.* **87**, 2458–2459 (1983).
29. Davies, M. B., Fitzner, M. & Michaelides, A. Routes to cubic ice through heterogeneous nucleation. *Proc. Natl Acad. Sci. USA* **118**, e2025245118 (2021).

Methods

In situ low-dose cryogenic TEM imaging

Using the in situ liquid-nitrogen-cooled cryo-TEM holder (ZEPTOOLS, PicoFemtoJN02), water vapour deposition was studied using aberration-corrected TEM. The microscope (JEOL, Grand ARM 300) was equipped with a pixel-detector-based ultralow-dose electron imaging camera (Gatan, K2) operated at an accelerating voltage of 300 kV. The temperature of the ultrathin substrate suspended on a TEM grid was set up with a resistive heater and measured using a thermocouple thermometer. For a normal column vacuum of around 4×10^{-8} torr with an ambient humidity of approximately 18%, ice started to form when supersaturation was reached at approximately 110 K. The spherical aberration was corrected to around 1 µm. The twofold astigmatism was corrected to roughly 0 nm. The coma and three-fold astigmatism were corrected to several nanometres. The TEM bright-field image was obtained at an overfocus of around 10 nm for a negative spherical aberration, which facilitates real-time imaging of atoms with low electron-scattering power as observed previously[30]. The measured high-resolution TEM resolution was 1.6 Å for real-space imaging and 1.1 Å for reciprocal space imaging.

Elastic and inelastic collisions of high-energy incident electrons with atom columns inherent in TEM electron diffraction imaging transfer an amount of energy E (in eV) given by the following equation[31]:

$$E = E_{\max} \sin^2(\theta/2)$$

$$E_{\max} = E_0(1.02 + E_0/10^6)/(465.7A)$$

where E_0 is the incident electron energy, A is the atomic mass number and θ is the electron deflection angle. For light-element atoms such as hydrogen and oxygen, the maximum transferred energy from the 300-kV incident electron is about 850 eV and 47 eV, respectively. This energy transfer increases the temperature of the well-dispersed crystallites on the TEM grid by a few degrees. For specimens with poor conductivity, electron beam irradiation can also cause charge accumulation, which in turn results in mass transport because of the movement of ions in the electric field and the accompanying image blurring and distortion. When the transferred energy exceeds the displacement energy (E_d), which is estimated[32] to be 0.5 eV per molecule for water on the surface and 2.4 eV per molecule for water molecules in the lattice, the molecules are displaced from the initial sites. Furthermore, the radiation damage of the displacement effect further causes mass loss, which hinders microscopy characterization. The dose rate and the total dose of the electron beam are the main factors of the irradiation effects. For example, previous TEM studies have confirmed that at 200 kV and approximately 100 K, a typical imaging dose such as 1×10^5 e^- Å^{-2} will cause mass loss[32], whereas a higher dose of around 4×10^6 e^- Å^{-2} results in simultaneous mass loss and structural transition[26]. The current study measurements were performed with a safe dose of approximately 240 e^- Å^{-2} for ice imaging in the current conditions.

A typical electron dose rate used for in situ TEM imaging was around 120 e^- Å^{-2} s^{-1} to minimize the radiation effect on water. Each image stack was obtained at 40 frames per second and then aligned and summed up to improve the signal-to-noise ratio. Furthermore, a band-pass filter was used in the images as aquired. Notably, the deposited ice remained in an amorphous state after continuous low-dose electron beam illumination from the initial stage, indicating the inhibitory effect of the electron beam on the nucleation of crystalline ice. When the shutter used for blocking the beam was turned on for most of the time before imaging, chain-like disordered clusters randomly spread across the substrate in the initial stage, followed by regular ice Ic lattice nucleation and aggregation. For the EELS background deconvolution, the Fourier ratio method was used to remove the plural scattering in the low- and high-loss spectra.

Sample preparation

Monolayer graphene or h-BN used as cryogenic substrate for water vapour deposition was grown using chemical vapour deposition and then transferred onto a lacey carbon-covered quantifoil gold TEM grid using a direct-transfer method as described previously[33,34]. Suspended ultrathin carbon with a thickness of 2 nm on a quantifoil gold grid demonstrated hydrophobic features. Some of the grids were etched by hydrogen plasma for 30 s to obtain a hydrophilic surface.

TEM image simulations

TEM image simulations were calculated with a multi-slice algorithm using the QSTEM[35] software with the following TEM image parameters: spherical aberration coefficient, approximately 1 µm; specimen thickness, 10 nm; overfocus, around 10 nm; semi-angle of beam convergence, 3.7 mrad; defocus spread, 2.5 nm.

Molecular dynamics set-up

To model the local structure of ice and its changes on electron annealing, molecular dynamics simulations were done using the coarse-grained mW water model[10,11,36,37]. All simulations were performed with the large-scale atomic or molecular massively parallel simulator code[38]. The canonical ensemble was sampled using a Nosé–Hoover thermostat with a relaxation time of 1 ps. The motion equations were integrated with a time step of 10 fs to obtain the structure of ice. Constant pressure and temperature ensembles were performed using an additional Nosé–Hoover barostat with a relaxation time of 2.5 ps to simulate the structural evolution. More than 100 ps equilibration simulations were carried out for all set-ups before the production run. Modelled systems contained 700–6,000 water molecules. They were finite-sized in the xy plane and periodic in the experimental imaging z direction. Size effects were considered using test systems of double/quadruple thickness and systems of double length in the xy direction. The temperature during the simulation was set to 100 K. For constant-pressure simulations, the pressure was computed by averaging the three diagonal components of the external stress tensor. In the local structure transition processes, the temperature was increased to around 300 K and then lowered to 100 K over a period of 1 ns. In a separate test, the heating rate was increased and the temperature was raised to 600 K. The result was consistent with the 300-K annealing run.

Data availability

The data generated and analysed in this study are included with the paper.

30. Zhu, L. et al. Visualizing anisotropic oxygen diffusion in ceria under activated conditions. *Phys. Rev. Lett.* **124**, 056002 (2020).
31. Egerton, R. F., Li, P. & Malac, M. Radiation damage in the TEM and SEM. *Micron* **35**, 399–409 (2004).
32. Heide, H.-G. Observations on ice layers. *Ultramicroscopy* **14**, 271–278 (1984).
33. Wang, L. et al. Microscopic kinetics pathway of salt crystallization in graphene nanocapillaries. *Phys. Rev. Lett.* **126**, 136001 (2021).
34. Wang, L. et al. Synthesis of honeycomb-structured beryllium oxide via graphene liquid cells. *Angew. Chem. Int. Ed.* **59**, 15734–15740 (2020).
35. Koch, C. T. *Determination of Core Structure Periodicity and Point Defect Density along Dislocations*. PhD thesis, Arizona State Univ. (2002).
36. Molinero, V. & Moore, E. B. Water modeled as an intermediate element between carbon and silicon. *J. Phys. Chem. B* **113**, 4008–4016 (2009).
37. Moore, E. B. & Molinero, V. Ice crystallization in water's "no-man's land". *J. Chem. Phys.* **132**, 244504 (2010).
38. Thompson, A. P. et al. LAMMPS - a flexible simulation tool for particle-based materials modeling at the atomic, meso, and continuum scales. *Comput. Phys. Commun.* **271**, 108171 (2022).

Acknowledgements This work was supported by the National Natural Science Foundation of China (51991344, 11974388, 11888101, U1932153, 11974001, and 11974024), National Key R&D Program of China (2021YFA1400204, 2021YFA1400500, and 2019YFA0307800), the Program from Chinese Academy of Sciences (XDB33030200, XDB33010400 and ZDYZ2015-1),

Beijing Natural Science Foundation (Z190011), and Guangdong Major Project of Basic and Applied Basic Research (2021B0301030002). L.W. is grateful for the support from the Youth Innovation Promotion Association of CAS (2020009). J.C. thanks the Shanghai Supercomputer Center and the Tianhe-1A Supercomputer Center for computational resources.

Author contributions L.W. and X.B. supervised the project. X.H., L.Liao, H.S. and J.W. performed the experiment. X.T., Z.X., W.W., L.W. and X.B. built the experimental set-up. K.L. performed the computational calculations. J.C., Y.J. and E.W. advised on the theoretical modelling. L.Liu advised the sample processing. L.W. and X.B. conceived the idea and wrote the manuscript with contributions from all authors.

Competing interests The authors declare no competing interests.

Additional information

Supplementary information The online version contains supplementary material available at https://doi.org/10.1038/s41586-023-05864-5.

Correspondence and requests for materials should be addressed to Lifen Wang, Ji Chen, Enge Wang or Xuedong Bai.

Peer review information *Nature* thanks Yoshiaki Sugimoto and the other, anonymous, reviewers for their contribution to the peer review of this work.

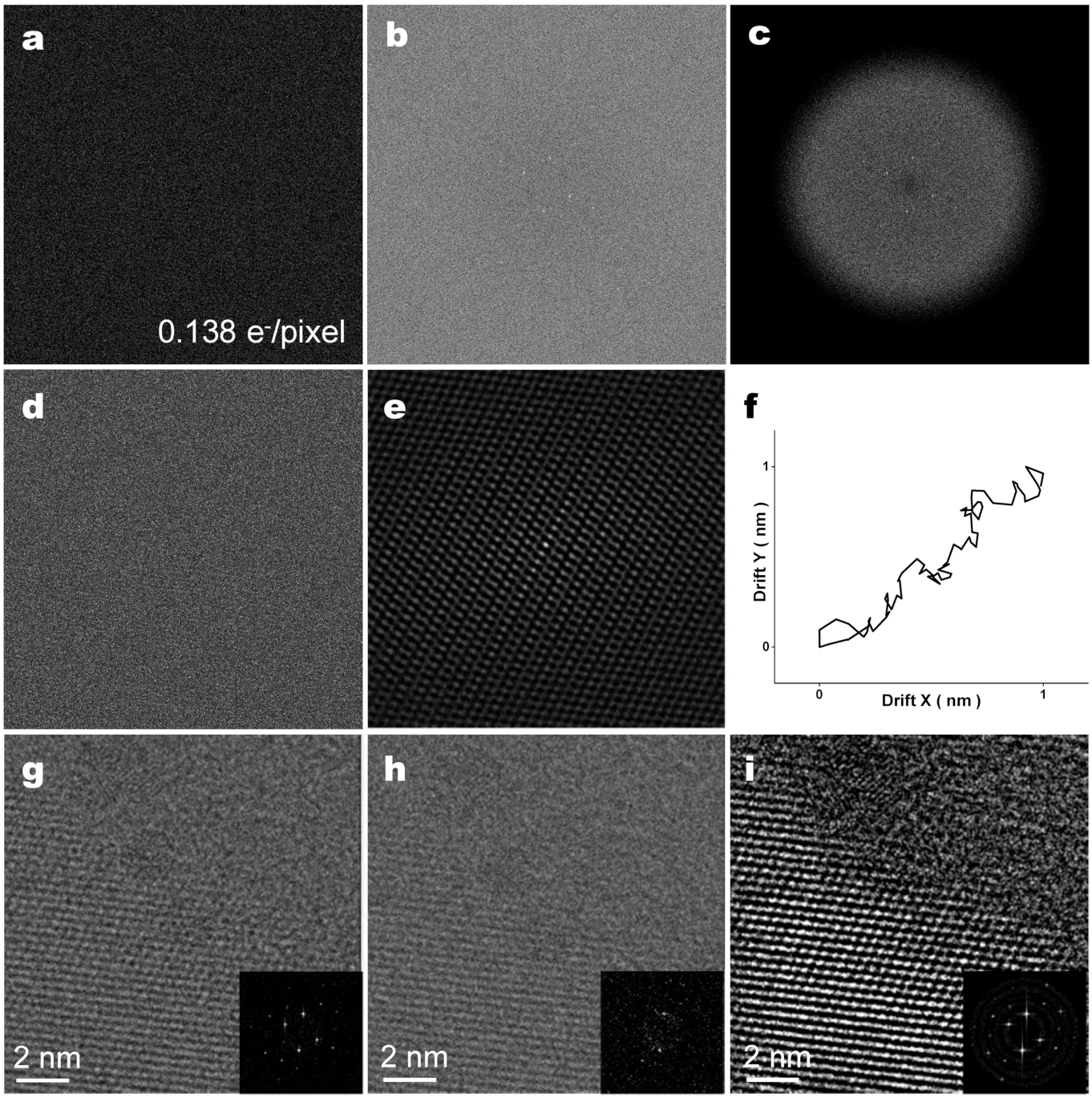

Extended Data Fig. 1 | Alignment and summing up of an image stack. **a**, A single frame in a TEM image stack (40 frames within an irradiation time of 2 s in total) obtained using single-electron counting mode via K2 camera with an electron beam dose rate of 196 e^{-}/Å^2/s. **b**, Corresponding FFT of image in (**a**). **c**, Band-pass filter. **d**, As-filtered TEM image of (**a**). **e**, Cross-correlation between one frame with (**a**) as the reference frame. **f**, Image-drift profile determined from filtered image using cross-correlations. **g**, Image acquired with eight drift-corrected frames from one stack binned together. **h**, Image formed by directly summing up all 40 frames without cross-correlations in the same stack as in (**g**). **i**, Image acquired by summing up eight frames from the same image stack used for images in (**g**) and (**h**) with combined band-pass filter and cross-correlation.

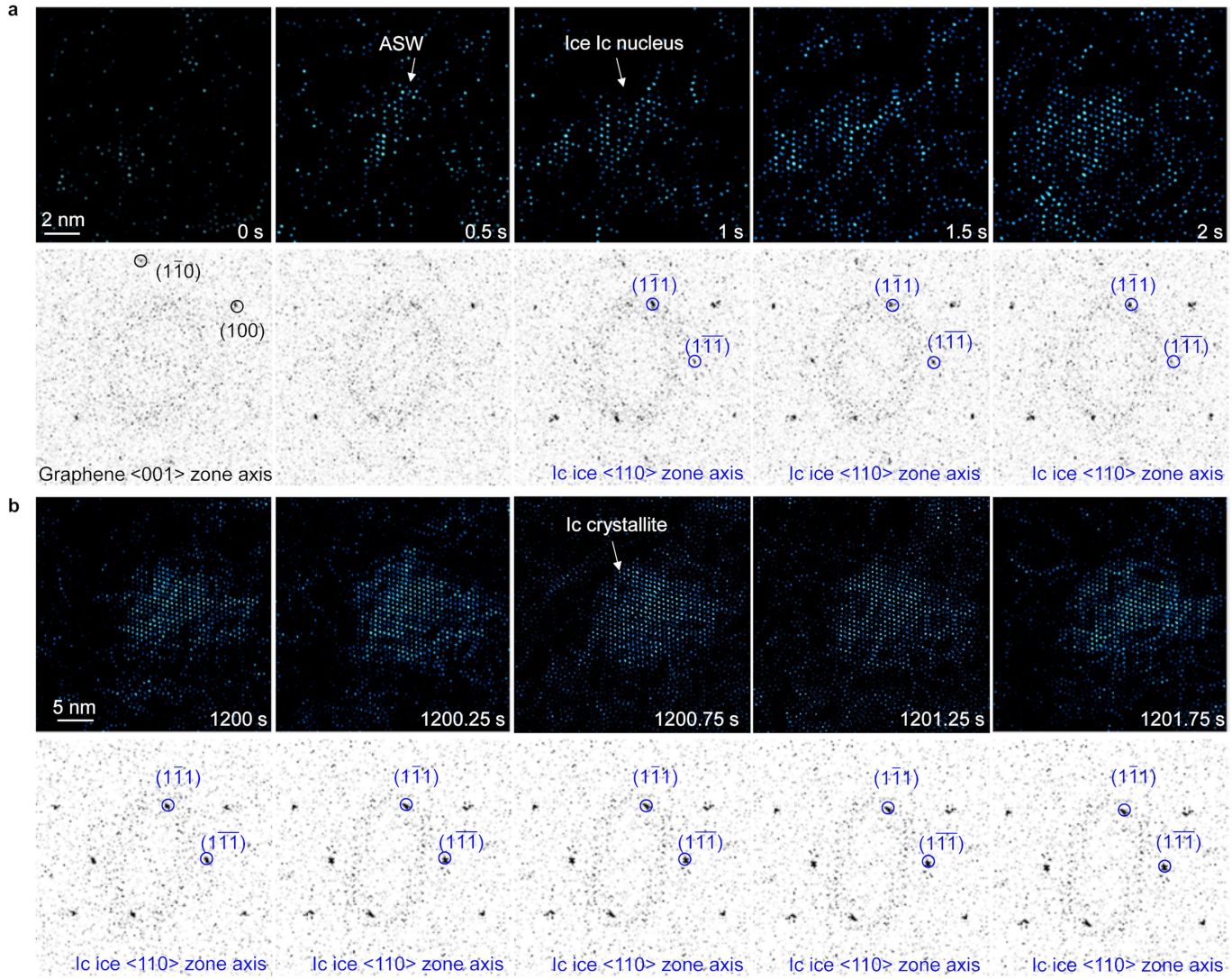

Extended Data Fig. 2 | Heterogeneous nucleation and growth of ice Ic. **a**, **b**, Snapshots of bright-field TEM images and corresponding FFTs used for tracking nucleation and crystallization of one Ic crystallite on graphene at about 102 K. Each image was obtained by summing eight aligned frames in one corresponding low-dose image stack acquired at a frame rate of 40/s with an irradiation time of 2 s and a dose rate of 156 e^{-}Å^{2}/s. Bright spots in the high-resolution images indicate water dimer column positions in lattices. *In-situ* images showed that ice-like clusters nucleated on substrate first, exhibiting amorphous features, and then aggregated to ice Ic nucleus, which gradually crystallized to form one nanometre-sized crystallite in about 20 min.

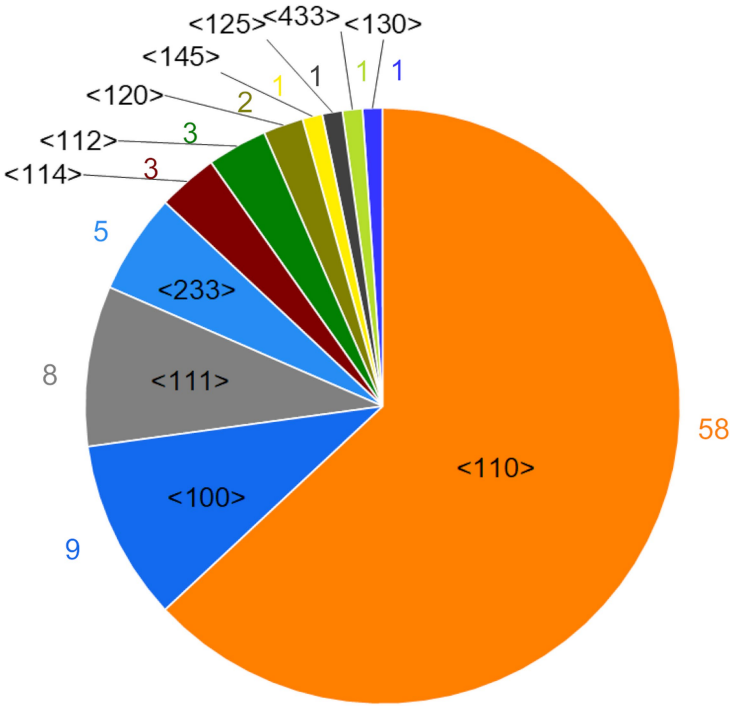

Extended Data Fig. 3 | Orientation statistics of ice Ic crystallites grown from vapour deposition on graphene at about 102 K. Orientation statistics of fully-grown ice Ic crystallites on one graphene substrate based on real-space measurements, showing ice Ic crystallites with a preference for <110> orientation. A total of 92 ice Ic crystallites with different crystallographic axis orientations were observed and measured using the same conditions on one graphene substrate. The orientation and the corresponding number of the ice Ic crystallites is annotated in the chart.

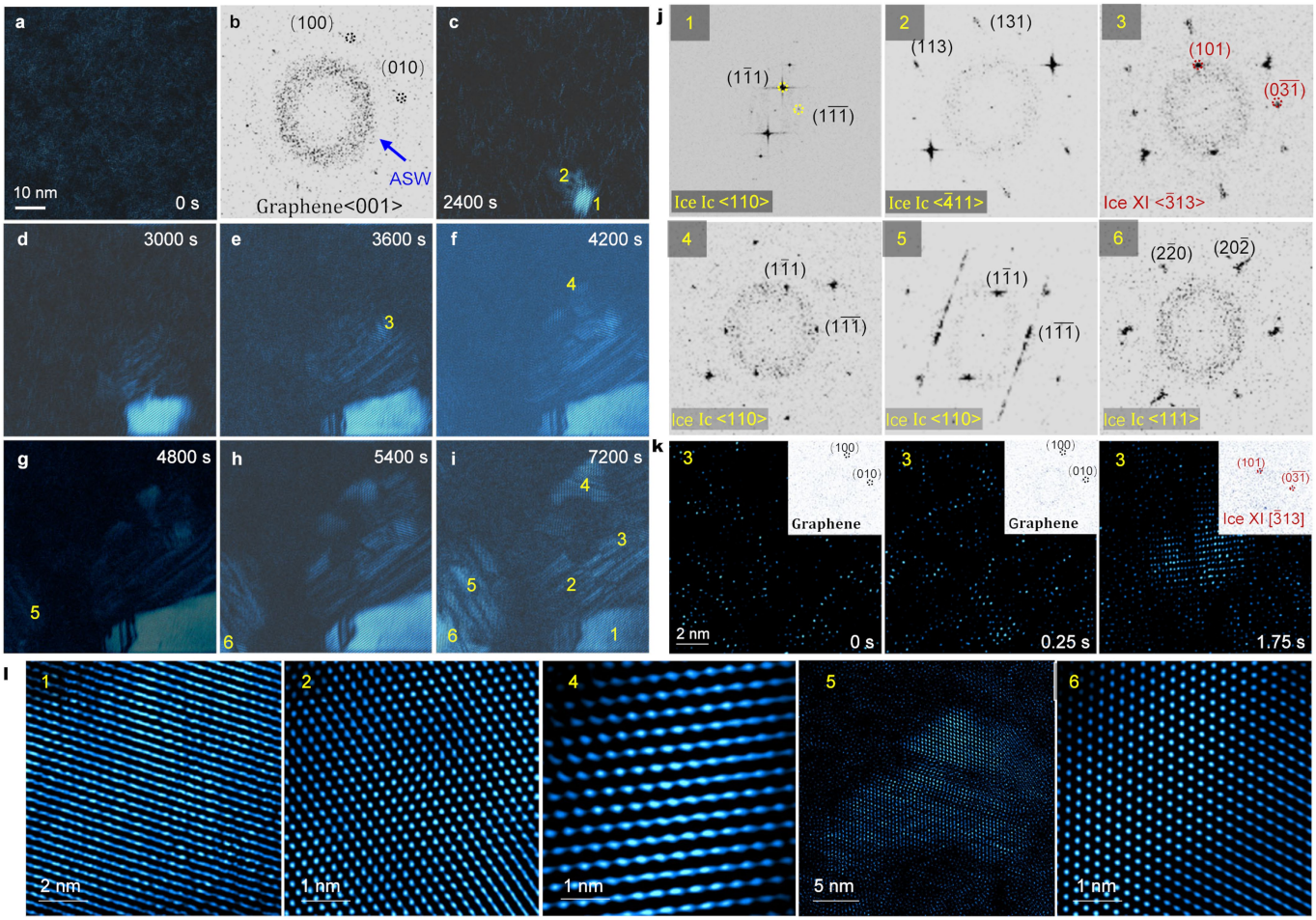

Extended Data Fig. 4 | Growth of ice Ic and ice XI crystallites. a–**i**, Snapshots of *in-situ* imaging showing the long-term ice deposition process. **b**, FFT of image in (**a**) demonstrated amorphous clusters formed on graphene in the initial deposition stage. Each image was obtained by summing eight aligned frames in one corresponding low-dose image stack acquired at a frame rate of 40/s and a dose rate of 108 e^{-}Å^{2}/s with an irradiation time of 0.4 s. Individual crystallites were numbered based on the order of nuclei appearance. **j**, Corresponding FFTs for different crystallites, showing five randomly oriented ice Ic structures (1, 2, 4–6) and one <$\bar{3}$13> crystallography zone axis-oriented ice XI (3). **k**, Snapshots of ice XI cluster. **l**, High-magnification micrograph of the respective crystallites. The out-of-plane growth direction of the crystallite one deviates slightly from the <110> axis, resulting in the high-magnification TEM image and corresponding FFT with low resolution.

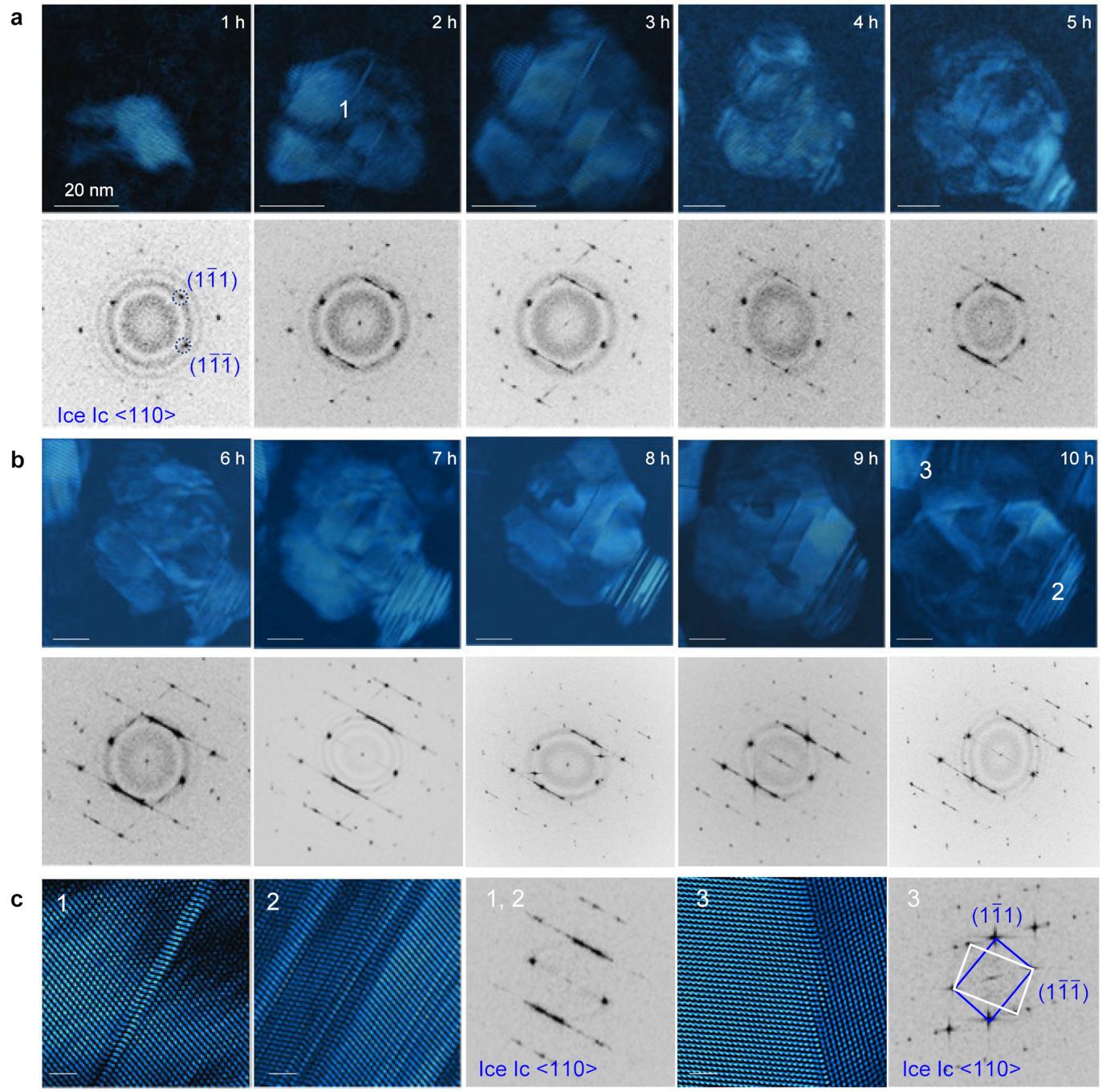

Extended Data Fig. 5 | Real-time growth process of ice Ic from vapour deposition at 102 K. a, **b**, Snapshots and corresponding FFT of *in-situ* imaging showing the long-term ice Ic growth process from vapour deposition. High density of defects on (1$\bar{1}$1) plane cause streaking in the diffraction spots of ice Ic crystallite. Liquid nitrogen was refilled to the Dewar of the cryo-holder every three hours to maintain a low temperature of 102 K. **c**, High-magnification image and corresponding FFT of defects in the ice Ic crystallite in (**a**) and another new ice Ic crystallite nearby showing the continuous nucleation and then crowded growth of ice Ic from prolonged vapour deposition. The crowded growth of multiple ice Ic crystallites result in multiple sets of diffraction spots to appear in the corresponding FFT of the TEM image. Each image was obtained by summing eight aligned frames in one corresponding low-dose image stack acquired at a frame rate of 40/s and a dose rate of 126 $e^{-}/Å^{2}/s$ with an irradiation time of 0.4 s. Scale bars, 20 nm for (**a**), (**b**); 2 nm for (**c**).

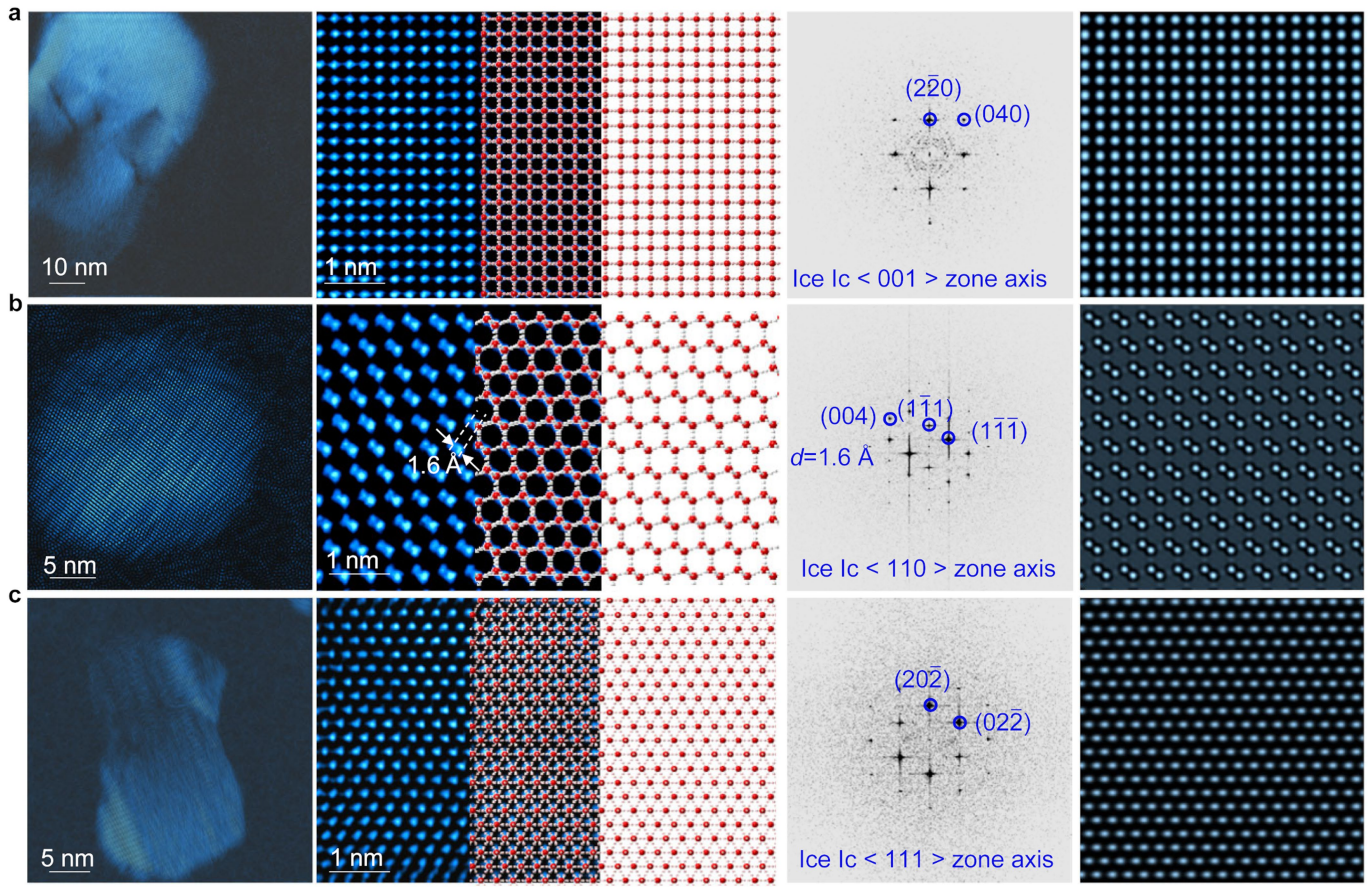

Extended Data Fig. 6 | Single-crystalline ice Ic crystallites grown by vapour deposition at 102 K. a–c, Low-magnification TEM image, high-magnification micrograph overlaid with atomic structure model, corresponding FFT, and computed TEM image of individual single-crystalline ice Ic crystallites oriented along <001>, <110>, and <111> zone axes, respectively. The smallest lattice spacing in real space is marked in the <110> image. The measured resolution for reciprocal space is also annotated in the FFT image. Electron beam dose: 50.8 $e^-/Å^2$ for (**a**), 47.6 $e^-/Å^2$ for (**b**); 37 $e^-/Å^2$ for (**c**). Electron beam irradiation time: 0.4 s for (**a–c**).

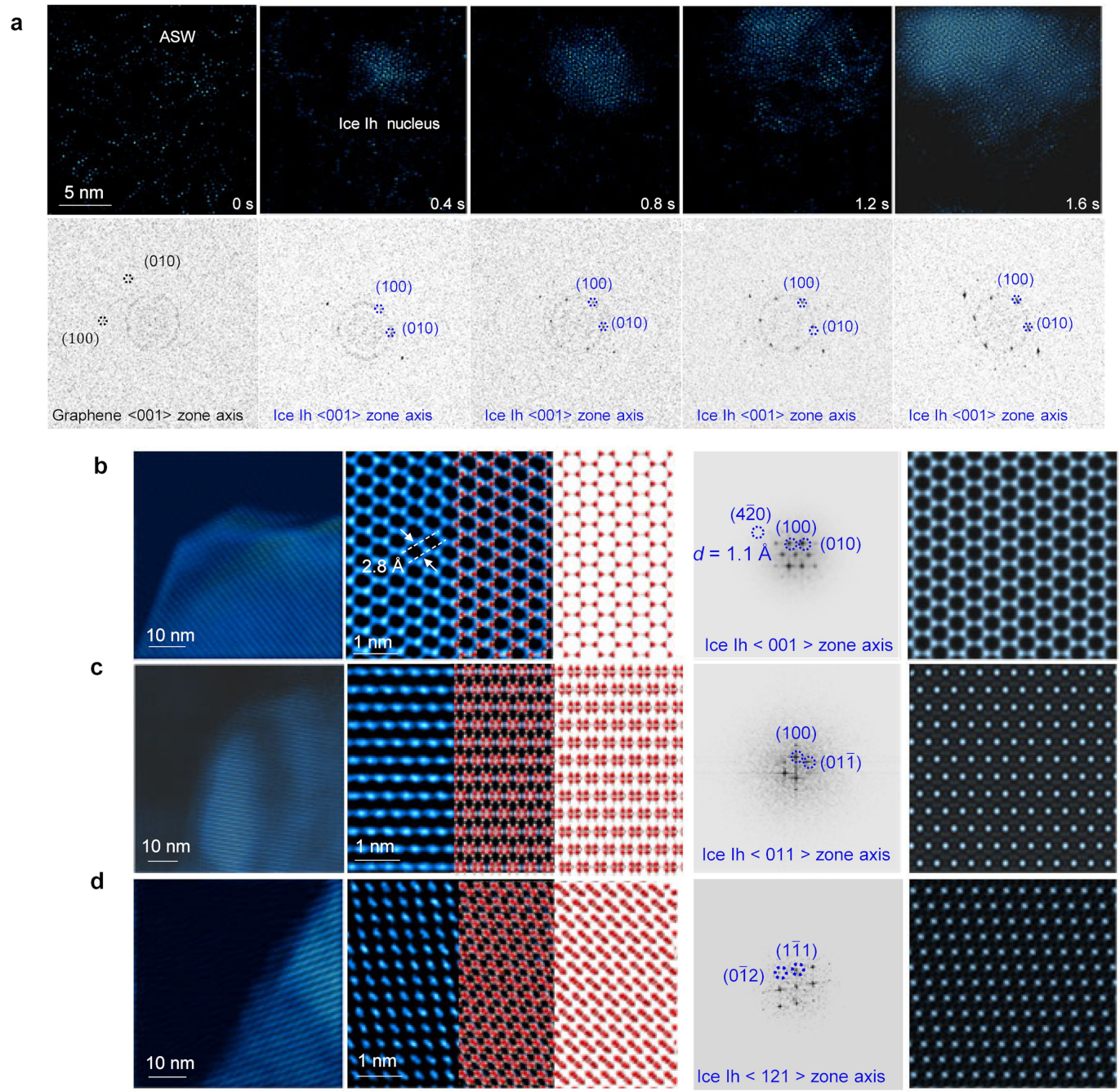

Extended Data Fig. 7 | TEM micrographs of ice Ih crystallite formation by vapour deposition at 102 K. a, Sequential micrograph showing heterogeneous nucleation of one <001>-oriented ice Ih. Start time was defined as the time when the observation started. Each image was captured at an electron dose rate of 119 $e^-/Å^2/s$ and a total dose of 47.6 $e^-/Å^2$. **b**–**d**, Low-magnification image, high-magnification image overlaid with atomic structure model, corresponding FFT, and computed image of separate ice Ih crystallite with a <001>, <011>, and <121> orientation, respectively. Illumination electron beam dose and time: ice Ih <001>, 50.4 $e^-/Å^2$ and 0.4 s; ice Ih <011>, 45.6 $e^-/Å^2$ and 0.4 s; ice Ih <121>, 43.2 $e^-/Å^2$ and 0.4 s.

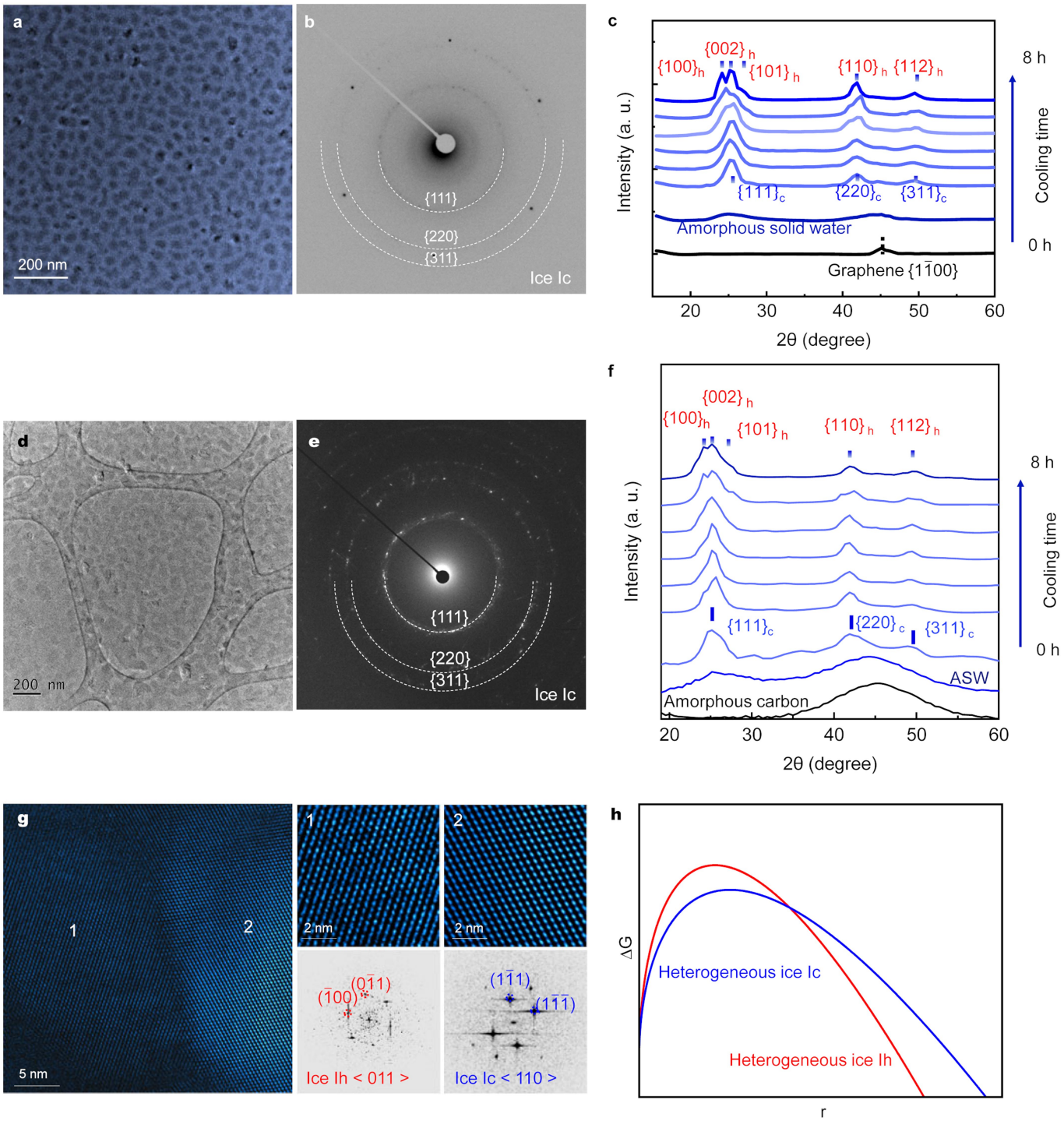

Extended Data Fig. 8 | Polymorphic ice I growth from vapour deposition at about 102 K. a–**c**, Low-magnification image, corresponding electron diffraction pattern, and diffraction intensity profiles of deposits from different randomly-selected micrometre-range areas at different time, showing structural variation of vapour deposition on graphene. Skewed diffuse Bragg peaks are labelled by ice Ic planes for the initial crystalline phase. Bragg peak positions for ice Ih, which also increase gradually with deposition time, are marked on the final intensity profile. The broadening and splitting of the diffraction peaks indicate the mixing of the two polymorphs. **d**–**f**, Low-magnification image, corresponding electron diffraction pattern, and electron diffraction intensity profiles of ice deposition on ultrathin carbon from different randomly-selected micrometre-range areas at different time, indicating mainly amorphous solid water giving way to ice Ic during the embryonic stages. Skewed diffuse Bragg peaks indicate unmistakable contribution of ice Ih. Shoulders around Ic {111} peak position are annotated with the relevant planes of ice Ih in red colour. **g**, Micrograph of a region where two polymorphs coexist, the respective high-magnification image and the corresponding FFT of the two polymorphic crystallites, showing one <011>-oriented ice Ih and one <110>-oriented ice Ic formed together by vapour deposition on graphene after cooling for 8 h at about 102 K. **h**, Quantitatively calculated heterogeneous free energy profiles as a function of the cluster size r of two polymorphs, showing the experimentally observed results where the ice Ic dominates the polymorphic heterogeneous nucleation events. Electron beam dose rate: ~240 $e^-/Å^2/s$ for (**a**)–(**f**). Irradiation time: 0.4 s for (**a**)–(**f**).

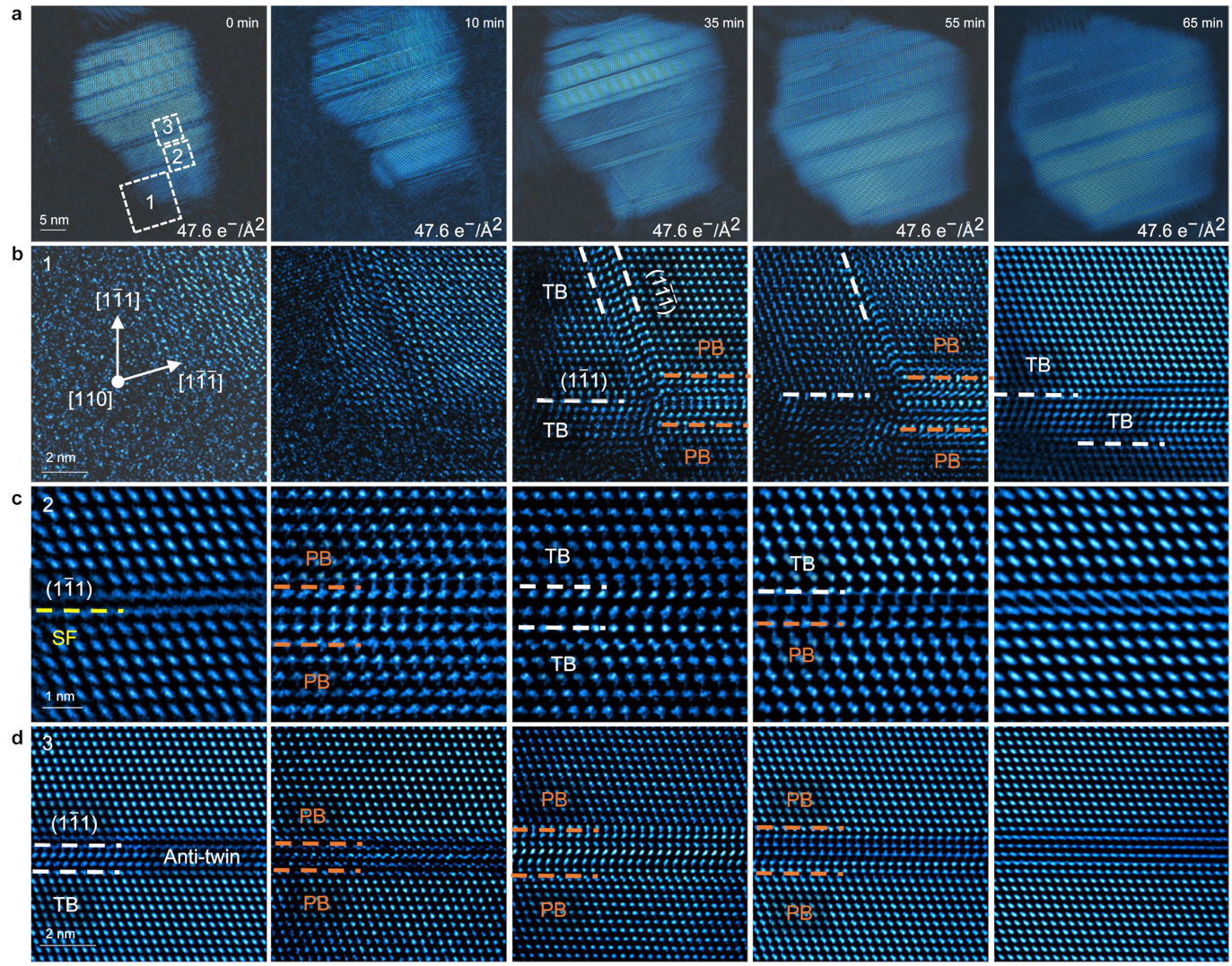

Extended Data Fig. 9 | Evolution of planar defects during ice Ic growth. **a**, Sequential TEM images of one defective ice Ic during growth. Illumination electron beam doses are annotated in each image. All images were obtained with an electron illumination time of 0.4 s. **b**–**d**, Zoom-in snapshot micrographs of different regions in (**a**) showing first aggregation and then annihilation of typical planar defects that are intermediate states to each other through slip planes in ice Ic during crystallite growth. Different defect types, including twin boundaries (TBs), stacking faults (SFs), and phase boundaries (PBs), are marked with dashed lines of different colours.

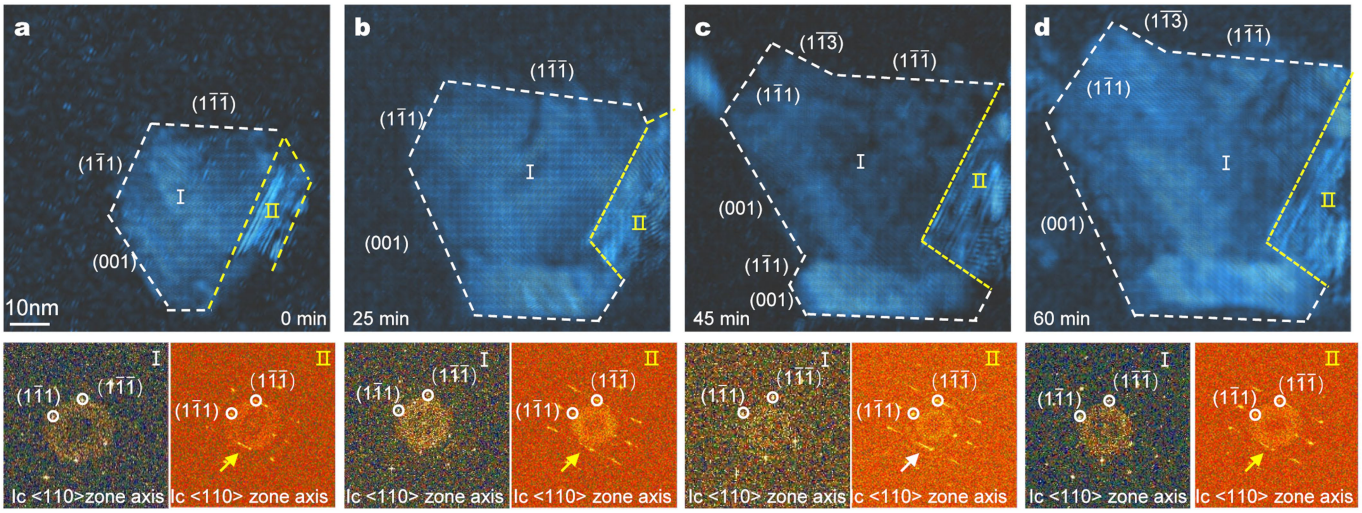

Extended Data Fig. 10 | Defective ice Ic growth. Growth of one defective ice Ic crystallite. a–**d**, Time-lapsed TEM images of one ice Ic crystallite (top row) and corresponding selected area FFTs (bottom row). The corresponding illumination electron beam dose of each image is 47 $e^-/Å^2$. Electron irradiation time for each image is 0.4 s. Facets were indexed as labelled on images. Area I is the single crystalline Ic matrix along <110> zone axis. Area II shows the high density of stacking faults on $(1\bar{1}1)$ plane based on diffractometry information. Both single-crystalline Ic matrix and the defected area grew over time with no phase transition during the observation time.